eScience 2 (2022) 606–614

Contents lists available at ScienceDirect

eScience

journal homepage: www.keaipublishing.com/en/journals/escience

Communication

Deformation-tolerant metal anodes for flexible sodium–air fiber batteries

Lei Ye [1], Xiangran Cheng [1], Meng Liao, Tiancheng Zhao, Xinlin Huang, Xinyue Kang, Kun Zhang, Xuemei Sun, Bingjie Wang [*], Huisheng Peng [*]

State Key Laboratory of Molecular Engineering of Polymers, Department of Macromolecular Science, and Laboratory of Advanced Materials, Fudan University, Shanghai 200438, PR China

HIGHLIGHTS

- A novel flexible sodiated carbon nanotube layer is fabricated through a Fermi level-driven spontaneous synthetic process.
- The sodiated carbon nanotube layer enables deformation-tolerant and flexible metal anodes.
- Novel fiber-shaped Na–air batteries with high flexibility and high electrochemical performance are constructed.

GRAPHICAL ABSTRACT

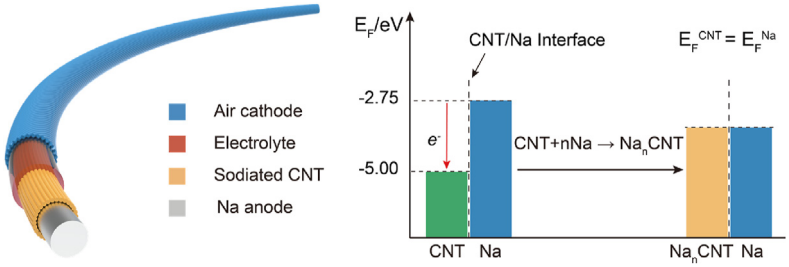

ARTICLE INFO

Keywords:
Sodium metal
Flexible battery
Sodium–air battery
Dendrite
Carbon nanotube

ABSTRACT

Although flexible sodium–air (Na–air) batteries with high theoretical energy density offer promising opportunities for next-generation smart electronics, enhancing the safety and efficiency of flexible sodium metal anodes under dynamic and continuous deformation remains a challenge. Here, a flexible sodiated carbon nanotube layer to suppress dendrite growth under various deformations is demonstrated through a Fermi level-driven spontaneous synthetic process. The resulting sodiated carbon nanotube layer, which has a spontaneously formed solid–electrolyte interface and a robust interlocked structure, creates a uniformly distributed electric field and stable interface even under deformation, affording dendrite-free flexible Na metal anodes. With this deformation-tolerant Na metal anode, we have constructed a new family of highly flexible Na–air fiber batteries with excellent cycling performance for 400 cycles at a current density of 1000 $mA{\cdot}g^{-1}$ and a capacity limit of 500 $mAh{\cdot}g^{-1}$ under dynamic deformation. These Na–air fiber batteries can be further woven into self-powering systems to support flexible electronic devices.

1. Introduction

The rapid development of portable and flexible electronics has necessitated a revolution in power supply systems in terms of high energy density and mechanical flexibility [1–3]. Non-aqueous and hybrid sodium–air (Na–air) batteries, which have high energy density (1108 $Wh{\cdot}kg^{-1}$), high nitrogen tolerance (important for ambient air applications), and low cost, are recognized as one of the promising candidates to power flexible electronic devices [4–6]. Thus far, much attention has been paid to developing sophisticated flexible cathodes and electrolytes that enhance the cycle life of flexible Na–air batteries to the required level [7,8]. However, problems with the Na metal anode impedes the realization of practical flexible Na–air batteries. Various deformations (e.g., bending, folding, and twisting) inevitably

* Corresponding authors.
E-mail addresses: wangbingjie@fudan.edu.cn (B. Wang), penghs@fudan.edu.cn (H. Peng).
[1] These authors contributed equally to this work.

https://doi.org/10.1016/j.esci.2022.10.001
Received 24 July 2022; Received in revised form 12 September 2022; Accepted 4 October 2022
Available online 7 October 2022

faced by flexible batteries easily crack or crease malleable Na metal, generating deposition "hotspots" at which the local electric field and sodium-ion (Na^+) flux surge, leading to aggravated dendrite growth (Fig. 1) [9–11]. Deformation also exacerbates the pulverization of the Na metal anode and the loss of electroactive Na, causing rapid performance degradation in flexible Na–air batteries [12].

To date, various approaches have been proposed to relieve the dendrite growth problem in Na metal anodes, including electrolyte engineering [8,13,14], artificial solid–electrolyte interfaces (SEI) [15,16], and nanostructured hosts [17,18]. Generally, these strategies mainly focus on conventional planar metal anodes in static application scenarios, with few considering the Na plating/stripping behaviors under dynamic deformation. Thus far, stable Na metal anodes with high flexibility have not been developed, retarding progress for flexible Na–air batteries. Considering that the electric field and the interface property control Na deposition, homogenizing the electric field and constructing a stable interface under various deformations are key to stabilizing flexible Na metal anodes [19,20].

Here, we have constructed a flexible Na metal anode stabilized by a sodiated carbon nanotube layer (SCL) formed in situ, which affords the fabrication of flexible Na–air fiber batteries with both high flexibility and high electrochemical performance. The SEI that forms spontaneously on the SCL once the carbon nanotubes (CNTs) are in contact with the Na metal in the electrolyte presents integrity and homogeneity against deformation to achieve a stable interface (Fig. 1b). Meanwhile, the interlocked CNTs create a mechanically robust structure that prevents the formation of cracks or creases on the anode surface during various deformations (Figs. 1a and d). As a result, a uniformly distributed electric field and a stable interface can be achieved even under deformation, rendering dendrite-free flexible Na metal anodes. With

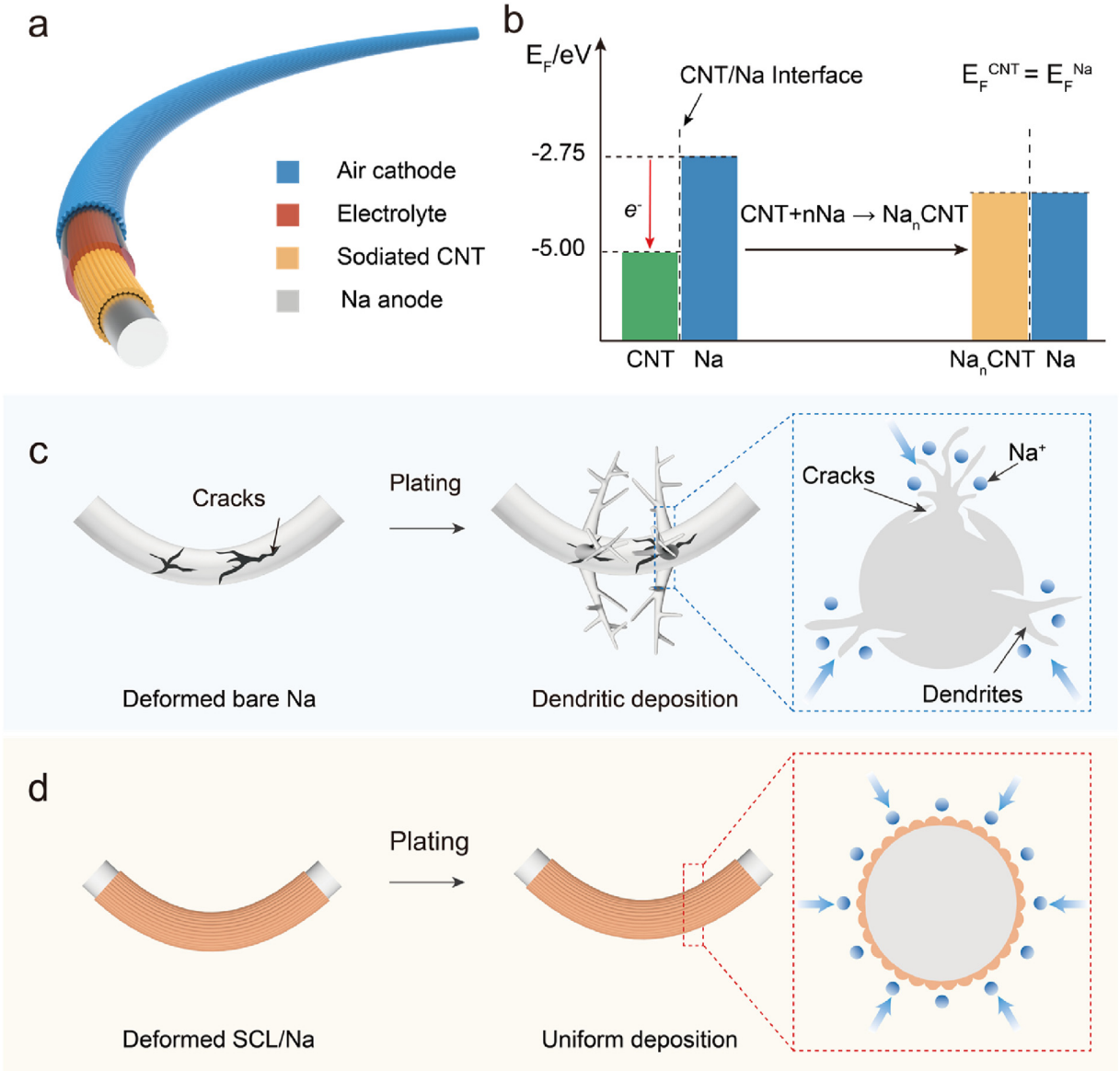

Fig. 1. (a) Schematic illustration of a SCL/Na–air fiber battery. (b) Energy diagrams demonstrate the spontaneous sodiation of CNT and the corresponding redox reaction driven by the difference in Fermi levels between CNT and Na metal. (c) Deformations faced by the Na–air fiber battery inevitably induce defects on the Na surface that cause a non-uniform electric field and consequent non-uniform Na deposition, leading to dendrites. (d) In the SCL/Na fiber anode, the mechanically robust structure of the SCL and the spontaneously formed SEI create a uniformly distributed electric field and stable interface even under deformation, rendering dendrite-free Na plating.

this deformation-tolerant Na metal anode, we have constructed a new family of Na–air fiber batteries with a high cycling performance of over 400 cycles (1000 mA·g^{-1} and 500 mAh·g^{-1}) and high flexibility.

2. Results and discussion

The flexible CNT film for the SCL was continuously prepared by a floating catalyst chemical vapor deposition method (Fig. S1) [21]. The film exhibited an interlocked structure with CNT bundles over 100 μm long, enabling excellent flexibility and mechanical strength (i.e., a tensile strength of 427 MPa and a Young's modulus of 3.2 GPa), which averted the generation of cracks or creases under various deformations (Figs. S2 and S3) [22]. Moreover, the film was porous and had a large specific surface area of 134.3 m^2·g^{-1}, helping reduce the local current density at the fiber anode surface, which is important for fiber batteries with a small electroactive area (Fig. S4).

The SCL on Na metal fiber was prepared by wrapping the metallic Na fiber with flexible CNT film and then wetting the composite electrode with an electrolyte of 1 M sodium trifluoromethanesulfonate (NaTF) in diglyme. Upon physical contact, the difference in Fermi levels (−2.75 eV for Na and −5.00 eV for carbon) yielded a contact potential of 2.25 V between Na and the CNTs (Fig. 1b). This contact potential drove the sodiation of CNT, i.e., spontaneous electrolyte decomposition formed the initial SEI on CNT bundles and prompted the intercalation of Na^+ into the CNT to achieve the Fermi level equilibrium (Fig. S5) [23,24]. This initially formed insulating SEI decreased the electrical conductivity of the sodiated CNTs [25]. Large amounts of O, F, Na, and S (the main components of the SEI), totaling 35.3 at%, were detected in the SCL by X-ray photoelectron spectroscopy (Fig. S6). Specifically, the initial SEI was composed of inorganic components (e.g., Na_2CO_3 and NaOH) derived from the NaTF salt and organic components (e.g., C–O, C–C/C–H, and COO-containing species) derived from the diglyme solvent (Fig. S7) [26]. Meanwhile, the flexible CNTs resulted in a SEI that was stable and uniform against cracking during deformation. In addition, the intercalated Na^+ in the SCL could be reversibly extracted and then refilled from the Na^+-containing electrolyte during Na deposition, facilitating homogeneous Na^+ distribution and transportation in the SCL (Figs. S8–S10) [25,27].

We explored the morphological evolution of the SCL/Na fiber electrode. The SCL/Na electrode exhibited a nearly unchanged diameter (~1.11 mm) compared with the bare Na fiber electrode (~1.03 mm), suggesting that the introduction of thin, lightweight SCL could minimize

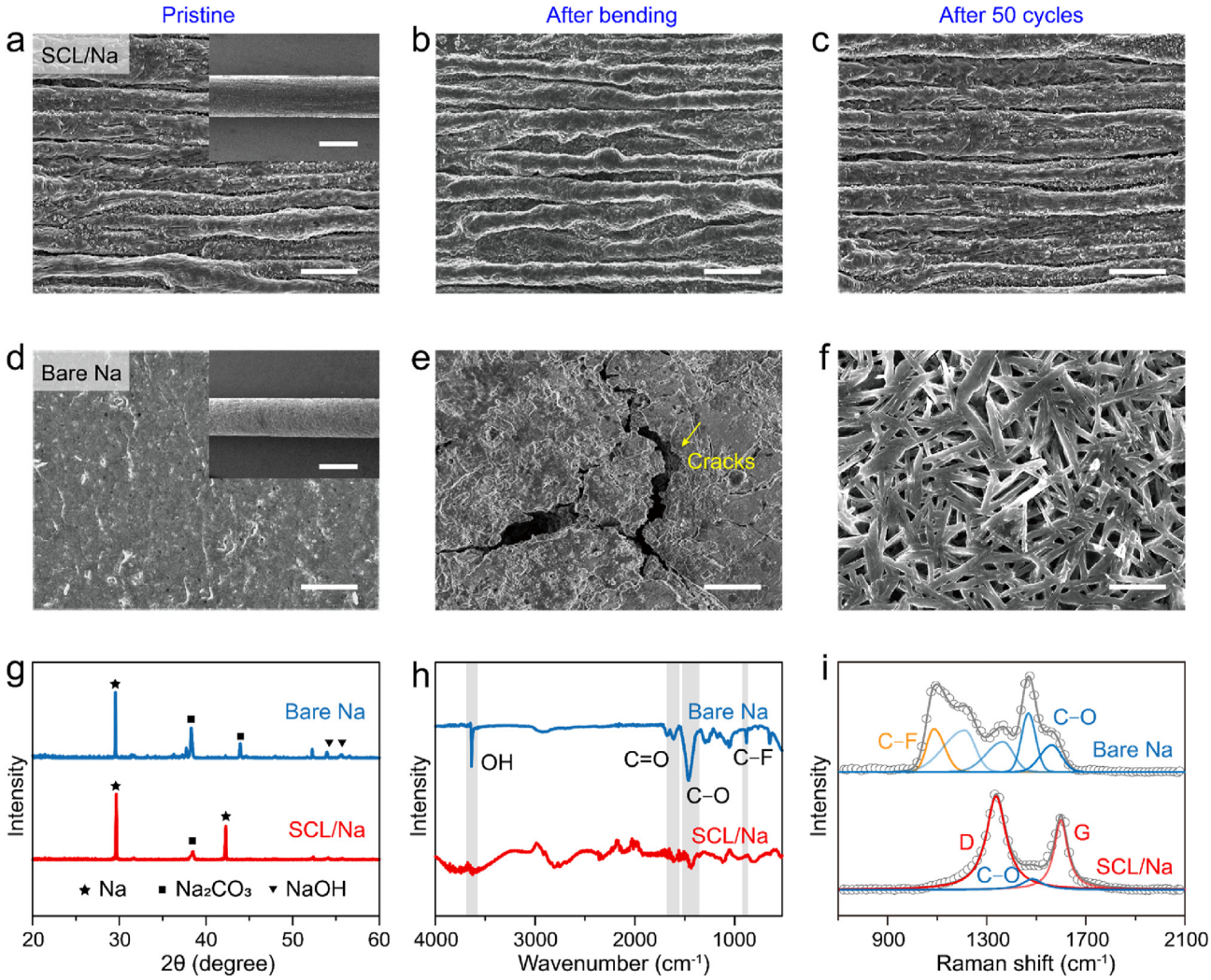

Fig. 2. (a–c) Scanning electron microscopy images of the SCL/Na fiber electrode in the pristine state (a), after ten cycles of bending at 90° (b), and then followed by 50 plating/stripping cycles at 1 mA·cm^{-2} and 1 mAh·cm^{-2} (c). Inset: low-magnification image of the SCL/Na fiber electrode. (d–f) Scanning electron microscopy images of the bare Na fiber electrode in the pristine state (d), after ten cycles of bending at 90° (e), and then followed by 50 cycles at 1 mA·cm^{-2} and 1 mAh·cm^{-2} (f). Inset: low-magnification image of the bare Na fiber electrode. Scale bars: 10 μm, and 1 mm for the inset. (g–i) X-ray diffraction patterns, Fourier transform infrared spectra, and Raman spectra of the SCL/Na and bare Na fiber electrodes after cycling, respectively.

the sacrifice of electrode capacity (Figs. 2a and d). Under severe deformation (e.g., ten cycles of 90° bending), no apparent wrinkle or crack was observed on the SCL/Na electrode, indicating uniform interfacial properties for the subsequent Na deposition (Fig. 2b). When the bent SCL/Na electrode was electrochemically cycled in symmetric cells at current densities of 1 and 5 mA·cm^{-2}, the macroscopically aligned morphology was well maintained, and no dendrites were observed (Figs. 2e and S11a).

After long-term cycling, whereby the detrimental impact of surficial defects was drastically exacerbated, a dendrite-free morphology was still observed for the SCL/Na electrode, verifying the effectiveness of SCL in stabilizing Na plating/stripping (Fig. S12a). In sharp contrast, the pristine, smooth surface of the bare Na metal fiber had deteriorated after bending deformation, showing apparent cracks and creases (Figs. 2d and e). These surficial defects served as deposition "hotspots" during recurring Na plating, leading to severe dendrite growth after only 50 cycles at 1 mA·cm^{-2}, not to mention at a higher current density of 5 mA·cm^{-2} (Figs. 2f and S11b).

Consistent with the compact and dendrite-free morphology of the SCL/Na electrode, improved interfacial properties were identified. After mechanical deformation (ten cycles of 90° bending) and electrochemical cycling for 50 cycles (1 mA·cm^{-2} and 1 mAh·cm^{-2}), the SCL/Na fiber electrode exhibited the dominant peaks of metallic Na in its X-ray diffraction pattern. In sharp contrast, the distinct peaks of side reaction products (e.g., Na_2CO_3 and NaOH) were observed for the bare Na fiber anode, due to severe side reactions between the reactive electrolyte and fresh Na continuously exposed by dendrite growth as well as electrode cracking (Fig. 2g) [8]. Much smaller peaks assigned to organic by-products (e.g., species containing C═O, C–F, and C–O) were also observed for the SCL/Na fiber electrode compared with the bare Na fiber electrode, according to the Fourier transform infrared spectra (Fig. 2h) [28]. More precisely, large proportions of F (12.94 at%) and S (4.57 at%) elements derived from the electrolyte were detected in the bare Na fiber electrode, as revealed by X-ray photoelectron spectroscopy (Fig. S13 and Table S2). By contrast, the SCL/Na electrode exhibited an almost unchanged proportion of F and S elements (5.96 at% in total) compared with 3.74 at% in the as-prepared electrode, verifying a stable interface that could withstand severe deformation [29]. These results confirmed that the SCL could effectively restrain side reactions of Na metal in the highly reactive electrolyte and reduce active Na loss. After repeated electrochemical cycling and mechanical deformation, the SCL retained a stable structure, as verified by the prominent D and G bands in the Raman spectra, which was beneficial for continuously stabilizing Na deposition during long-term cycling (Figs. 2i and S14).

To further understand the Na deposition process with SCL, finite element simulations were conducted on the fiber Na anodes (Fig. S15). Upon plating, Na^+ in the electrolyte quickly migrated toward the surface of metallic Na, driven by the electric field. For the soft and malleable bare Na electrode, deformation inevitably generated defective sites on the metal surface, e.g., cracks, creases, and protuberances. The local electric

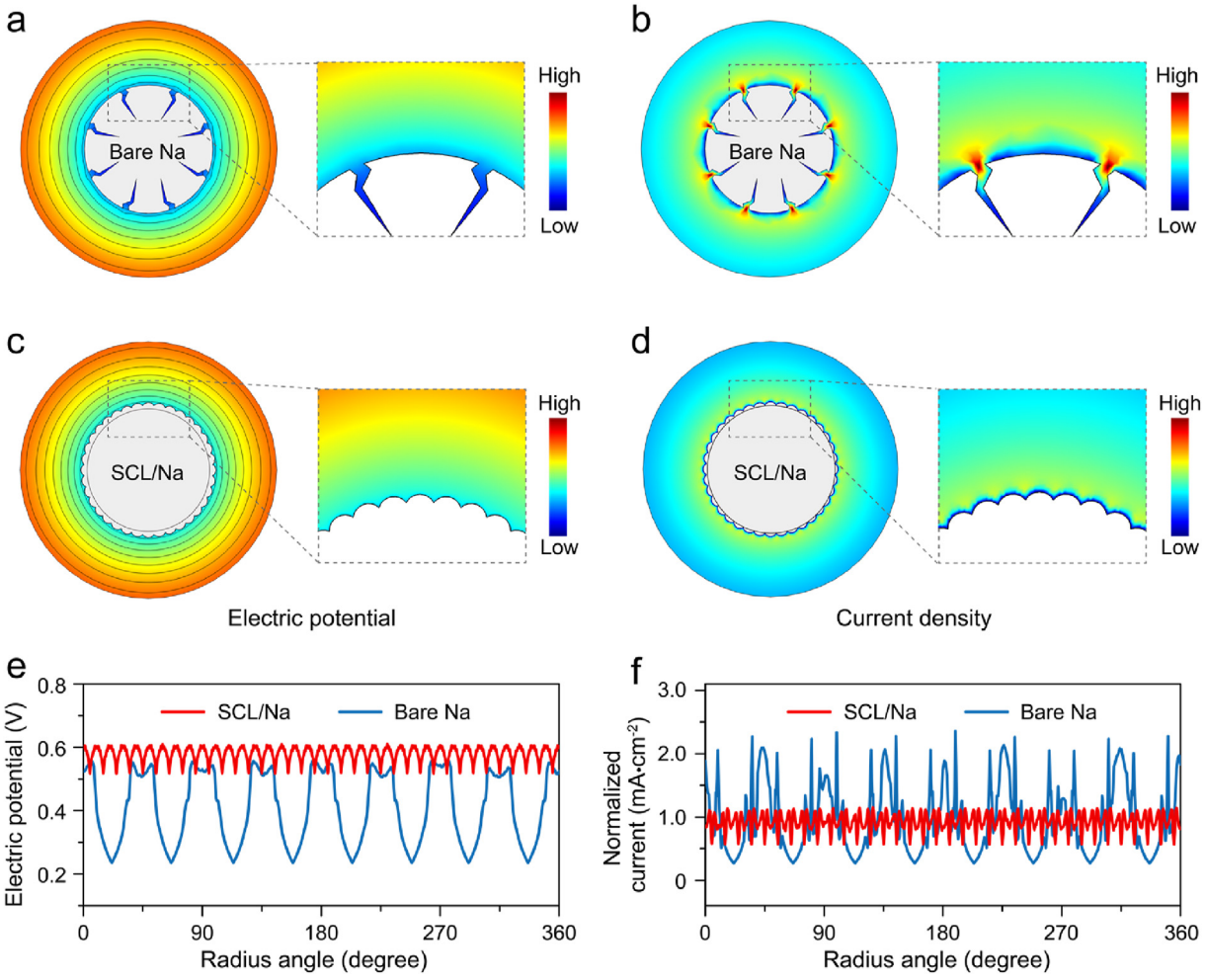

Fig. 3. (a, b) Electric potential and current density distributions, respectively, in the bare Na fiber electrode, determined by COMSOL Multiphysics simulation. (c, d) Electric potential and current density distributions, respectively, in the SCL/Na fiber electrode. (e) Electric potential profiles along the SCL/Na and bare Na surface, extracted from (a) and (c). (f) Current density profiles at the SCL/Na and bare Na surface, extracted from (b) and (d).

field was drastically intensified at these sites compared with the neighboring regions, as revealed by the large bumps in the electric field profile (Figs. 3a and e). Consequently, excessive Na^+ was attracted to these sites (Figs. S16a and S17), leading to sharp surges in local reaction currents and uncontrollable dendrite propagation (Figs. 3b and f). In contrast, in the SCL/Na fiber electrode, a uniform electric field distribution along the fiber electrode surface was obtained (Figs. 3c and e), due to its smooth and compact morphology. This uniform electric field contributed to an evenly distributed Na^+ flux and a homogeneous current density distribution on the SCL/Na electrode surface, yielding uniform Na deposition without dendrites (Figs. 3d, S16b, and S17) [30]. Meanwhile, the local current density in the SCL/Na fiber electrode was reduced, as visualized in the profile of the reaction current density; this was important for the co-axially structured fiber batteries, which had a much smaller geometric area than conventional planar ones (Figs. S18 and S19).

To investigate the effect of the SCL on the electrochemical performance of Na metal anodes, symmetric batteries based on the SCL/Na or bare Na electrodes were first cycled without bending deformation. With varied current densities of 1 and 5 $mA{\cdot}cm^{-2}$ at an areal capacity of 1 $mAh{\cdot}cm^{-2}$, the overall voltage profiles of the SCL/Na electrode indicated steady Na plating/stripping behaviors up to 1000 h, with regular voltage plateaus. In sharp contrast, after less than 250 h of cycling, the bare Na electrode under the same conditions of randomly fluctuating voltage profiles experienced severe dendrite growth and a deteriorated interface, in the absence of regulation by the SCL (Figs. S20 and S21) [26].

The SCL/Na and bare Na fiber electrodes were repeatedly bent to probe their electrochemical performance under severe deformation. Impressively, the deformed SCL/Na electrode delivered a cycling performance comparable to that without bending. Stable plating/stripping for over 800 h at 1 $mA{\cdot}cm^{-2}$ and 1 $mAh{\cdot}cm^{-2}$ was obtained, along with a steady voltage hysteresis of ~40 mV, suggesting the SCL effectively stabilized the electrode interface and restrained dendrite growth, even under deformation (Figs. 4a and S22a). For the bare Na electrode,

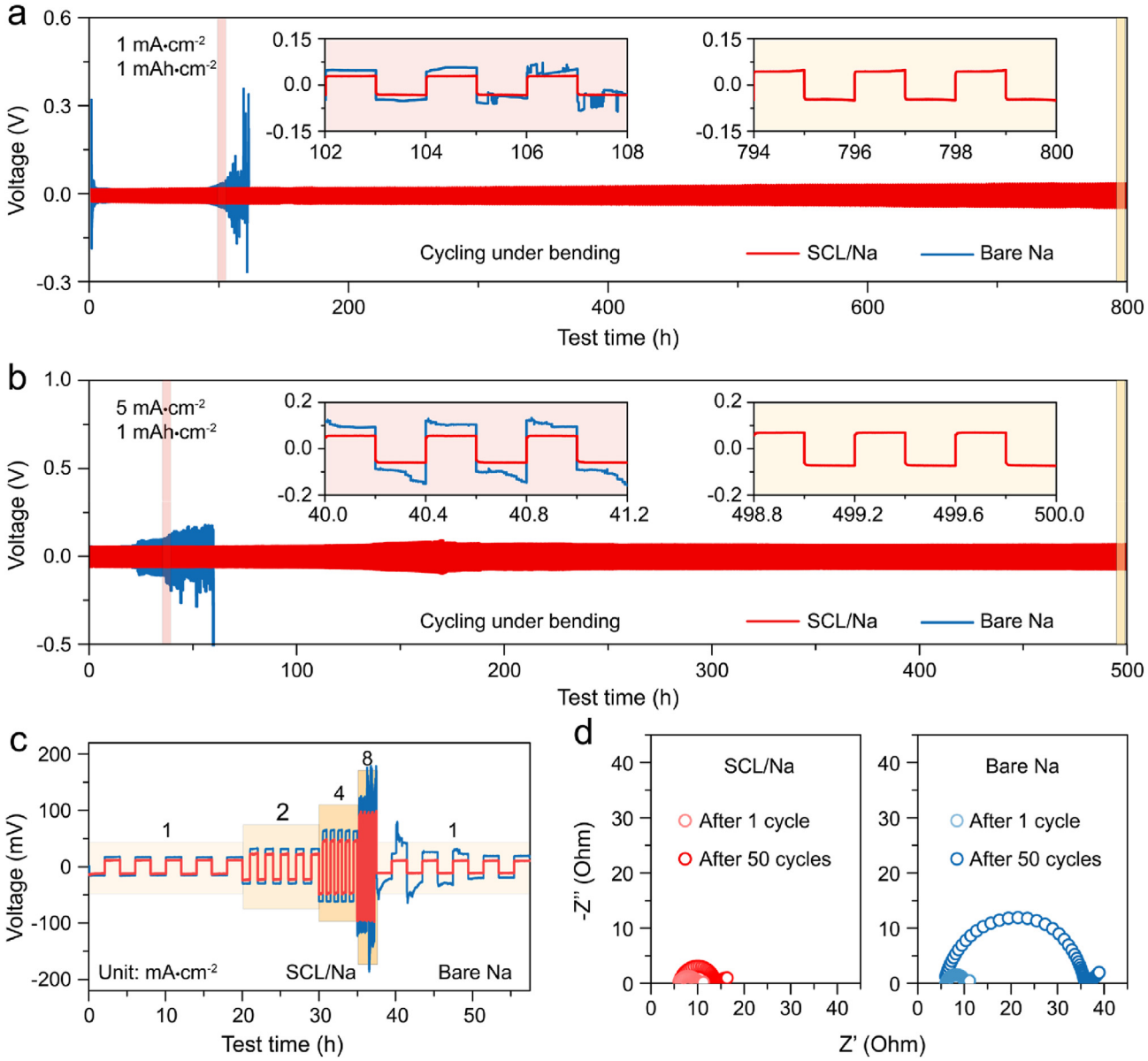

Fig. 4. (a and b) Galvanostatic cycling profiles of SCL/Na and bare Na electrodes at 1 $mA{\cdot}cm^{-2}$ and 1 $mAh{\cdot}cm^{-2}$ (a) and 5 $mA{\cdot}cm^{-2}$ and 1 $mAh{\cdot}cm^{-2}$ (b). (c) Rate performance of the SCL/Na and bare Na electrodes at current densities ranging from 1 to 8 $mA{\cdot}cm^{-2}$. (d) Nyquist plots of the SCL/Na (left panel) and bare Na (right panel) electrodes after 1 and 50 cycles.

cycling performance declined sharply to only ~100 h, which was 40% of the duration for the unbent one, due to aggravated dendrite growth under deformation. Studies at a higher current density (e.g., 5 $mA{\cdot}cm^{-2}$) showed stable Na plating/stripping for over 500 h (1250 cycles) with the SCL/Na electrodes, while the bare Na electrodes failed after ~50 h (Figs. 4b and S22b). The stable interfacial properties of the SCL/Na electrode were further proven by continuous cycling with current densities from 1 to 8 $mA{\cdot}cm^{-2}$. The overpotential of the SCL/Na fiber electrode was only marginally increased at high rates and recovered with reversal, while a larger overpotential at each rate was observed for the bare Na electrode (Fig. 4c). After repeated cycling, the interfacial resistance of the SCL/Na electrode increased from the initial 4.6–8.1 Ω. Note that the impedance of the bare Na electrode was 30.3 Ω after cycling, suggesting severe interfacial side reactions (Fig. 4d).

With the deformation-tolerant and dendrite-free SCL/Na fiber anode, a flexible Na–air fiber battery with a co-axial structure was successfully constructed by combining a flexible CNT film cathode and a gel electrolyte, to prevent electrolyte leakage during battery deformation (Fig. S23). The obtained SCL/Na–air fiber battery exhibited a typical diameter of ~0.5 cm and a length of ~15 cm (Fig. S24). The successful construction of Na–air fiber batteries was verified by the X-ray diffraction pattern of the discharged cathode, which showed the characteristic peaks of NaO_2 at ~32.5° and 46.5° (Figs. 5a and S25) [5]. After recharge, the NaO_2 was fully decomposed to re-expose the air cathode, confirming the reversible battery reaction of $Na + O_2 = NaO_2$ (Figs. S25 and S26). The fiber battery exhibited a discharge plateau at ~2.2 V and a flat charge curve, in accordance with a typical Na–air battery using sodium iodide as the redox mediator in the electrolyte [31,32]. The SCL/Na–air fiber battery exhibited an outstanding cycling performance of over 400 cycles, with stable discharge/charge voltage profiles as well as steady discharge plateaus at ~2.2 V (500 $mAh{\cdot}g^{-1}$ and 1000 $mA{\cdot}g^{-1}$) (Figs. S27a and S27c). Notably, this performance exceeded that of Na–air batteries reported in the literature (Fig. S28 and Table S3).

When cycled after repeated deformation (i.e., bending for ten cycles at a 90° angle), the SCL/Na–air fiber battery presented a cycling performance of 400 cycles, comparable to that of unbent fiber batteries, evidencing its structural stability and deformation endurance (Figs. 5a and c). In sharp contrast, the Na–air battery with a bare Na fiber anode suffered rapid performance decay within 90 cycles (Figs. S27b and S27c) and exhibited a poor performance of less than 30 cycles under deformation (Figs. 5b and c). Advantageous rate performance was obtained for the SCL/Na–air fiber battery, with stable discharge plateaus from 2.32 to 2.15 V at current densities ranging from 100 to 2000 $mA{\cdot}g^{-1}$ (Fig. S29). To understand the high performance of the SCL/Na–air fiber battery, the morphology of the Na fiber anodes after cycling was studied. As expected, a compact and dendrite-free morphology was observed for the SCL/Na fiber anode, while lots of dendrites appeared on the bare Na fiber anode, illustrating the effectiveness of the SCL for dendrite inhibition and correspondingly better performance (Fig. S30).

Besides its outstanding electrochemical performance, the SCL/Na–air fiber battery also presented a high flexibility that would satisfy

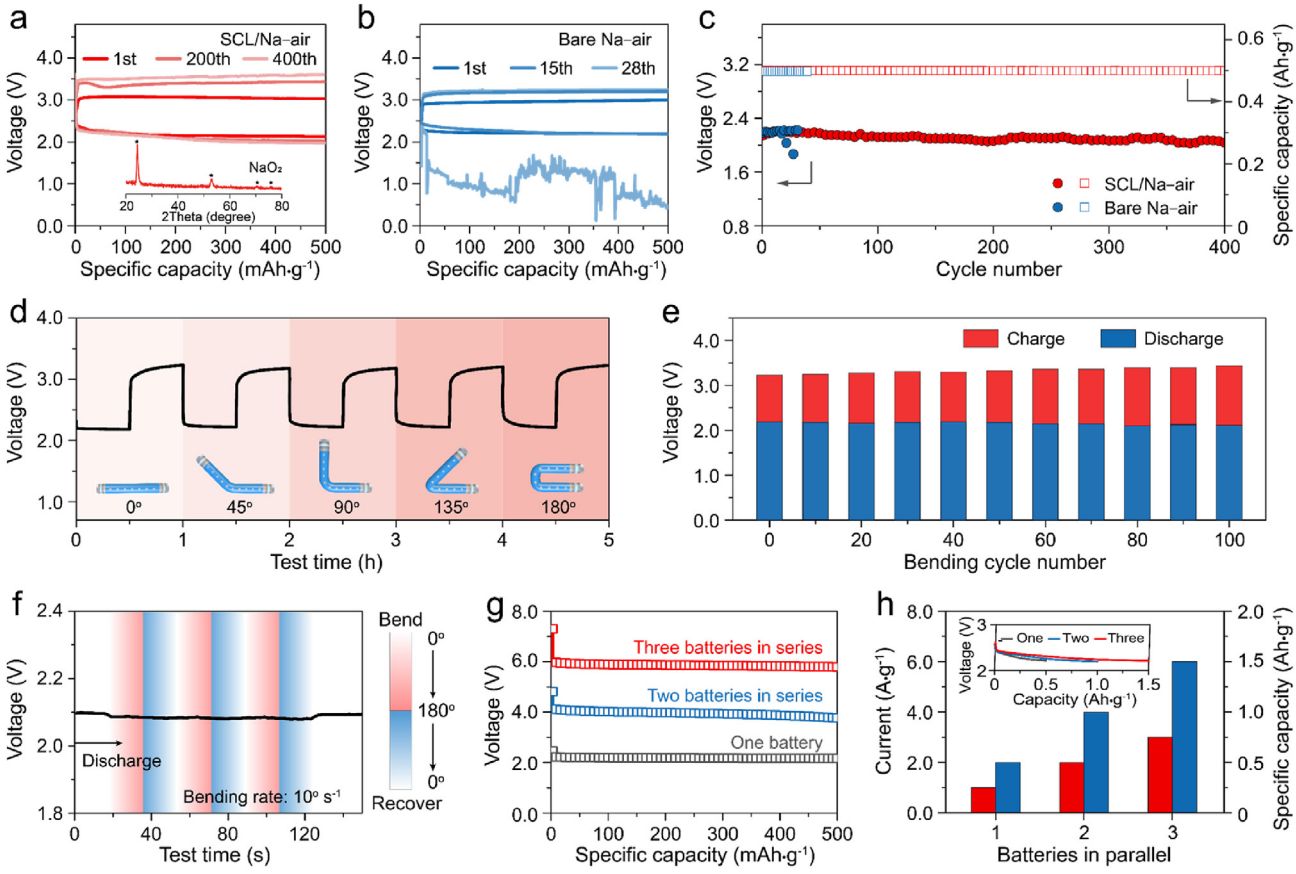

Fig. 5. (a) Discharge/charge voltage profiles of the Na–air fiber battery with SCL/Na fiber anode at 1000 $mA{\cdot}g^{-1}$ and 500 $mAh{\cdot}g^{-1}$ (inset: the X-ray diffraction pattern of the air cathode after discharging showed the discharge product was NaO_2). (b) Discharge/charge voltage profiles of the Na–air fiber battery with bare Na fiber anode at 1000 $mA{\cdot}g^{-1}$ and 500 $mAh{\cdot}g^{-1}$. (c) The corresponding discharge voltage plateaus for the two types of fiber batteries. (d) Discharge/charge voltage profiles of the SCL/Na–air fiber battery under increasing bending angles. (e) Dependence of discharge/charge voltage plateaus on bending cycle with a bending angle of 180°. (f) Discharge curve of SCL/Na–air fiber battery under a dynamic bending and releasing process. (g) Discharge curves of series-connected SCL/Na–air fiber batteries. (h) Currents and capacities of parallel-connected SCL/Na–air fiber batteries (inset: the corresponding discharge voltage profiles).

requirements for use in wearable electronic devices. It could be bent at a series of angles ranging from 0 to 180° while maintaining stable discharge/charge voltage profiles (Fig. 5d). Moreover, the internal battery resistance and polarization were not aggravated during 100 cycles of repeated bending at an angle of 180°, indicating the battery's structural stability (Fig. 5e). Under dynamic deformation (i.e., continuous bending at a rate of $10°{\cdot}s^{-1}$) that imitated complex application scenarios, the recorded voltage undulation of the SCL/Na–air fiber battery was less than 1% (Fig. 5f). In addition, these batteries could be connected in series or in parallel to expand their output voltage or capacity enough to meet the practical energy demands of electronic devices. For instance, three in-series fiber batteries could deliver a discharge plateau of over 6 V, and three in-parallel fiber batteries could achieve a threefold enhanced capacity (Figs. 5g and h). As a demonstration, the flexible SCL/Na–air fiber battery could steadily power up a digital timer in various deformation states (Fig. S31). We also fabricated a wearable self-powering stress-sensing system with an energy harvesting unit of fiber solar cells, an energy storage unit of SCL/Na–air fiber batteries, and a fiber strain sensor (Figs. S32 and S33).

3. Conclusions

In conclusion, an effective and scalable strategy for making flexible, high-performance Na–air fiber batteries has been demonstrated using a layer with a spontaneously formed SEI and a robust interlocked structure. This contributes to creating a uniform electric field and stable interface, even under dynamic and severe deformation, thereby enabling stable and dendrite-free Na metal anodes for flexible Na–air batteries. The as-fabricated Na–air fiber batteries exhibit outstanding cycling performance across 400 cycles, even under deformation. This work offers an efficient approach for developing high-performance metal–air batteries with high flexibility.

4. Materials and methods

4.1. Materials

Sodium metal (Na, 99.8%), sodium trifluoromethanesulfonate (NaTF, CF_3SO_3Na, 98%), diethylene glycol dimethyl ether (diglyme, $C_6H_{14}O_3$, 99.5%), trimethylolpropane ethoxylate triacrylate (average Mn of ~428), poly(vinylidene fluoride-*co*-hexafluoropropylene (average Mn of ~130,000), and 2-hydroxy-2-methylpropiophenone ($C_{10}H_{12}O_2$, 97%) were purchased from Sigma-Aldrich Co. Ltd. Ethanol (C_2H_6O, 99.7%) and sodium iodide (99%) were obtained from Sinopharm Co. Ltd. Ferrocene ($C_{10}H_{10}Fe$, 99%), thiophene (C_4H_4S, 99%), and N-methyl-2-pyrrolidinone (C_5H_9NO, 99.9%) were purchased from Aladdin Co. Ltd. Parafilm was purchased from Bemis Co. Ltd. Celgard 2400 separator was purchased from Celgard Co. Ltd. Heat shrinkable tubes were purchased from Suzhou Dasheng Materials Tech Co. Ltd.

4.2. Preparation of carbon nanotube film

The carbon nanotube (CNT) film used in this work was prepared by a floating catalyst chemical vapor deposition method. A composite catalyst of ferrocene (2 wt%) and thiophene (2 wt%) was well dispersed in an ethanol carbon source and pumped into a furnace at a steady flow rate of $10\ mL{\cdot}h^{-1}$. Meanwhile, a mixture of hydrogen and argon (4:1, v/v) was flowed across the furnace at a rate of 1500 sccm. Then the ethanol was decomposed to produce carbon atoms, and CNTs were generated in a reducing atmosphere of hydrogen under the above synthetic conditions. Finally, the CNTs were blown to the bottom of the furnace by the gas and pulled out with a stick. After a water coagulation bath for contraction, the CNTs were wound around a roller and dried in ambient air to form a porous CNT film. The resulting CNT film was composed of CNT bundles with a relatively long length of ~100 μm and exhibited a macroscopically aligned structure.

4.3. Fabrication and electrochemical measurements of sodiated CNT layer-protected Na fiber electrodes

To prepare sodiated CNT layer (SCL)/Na composite fiber electrodes, the Na metal fiber was wrapped with flexible CNT film and wetted with an electrolyte of 1 M NaTF in diglyme in an argon-filled glove box ($H_2O < 0.1$ ppm, $O_2 < 0.1$ ppm). The SCL was obtained via the physical contact and spontaneous reaction between metallic Na and CNTs, driven by the difference in their Fermi levels. To evaluate the anodic electrochemical performance, symmetric cells were assembled from SCL/Na and bare Na fiber electrodes. Each cell was assembled in an argon-filled glove box ($H_2O < 0.1$ ppm, $O_2 < 0.1$ ppm) with ~30 μL of electrolyte (1 M NaTF in diglyme) and using Celgard 2400 as the separator. The electrolyte was dried with molecular sieves (4 A) for 24 h before use. To investigate the cycling stability, the symmetric cells were tested under a galvanostatic plating and stripping process on a LAND-CT2001A battery tester. The unique one-dimensional Na fiber anode with a small diameter effectively avoided the use of excessive Na metal and enabled high utilization efficiency. Electrochemical impedance spectroscopy was measured on a CHI 660D electrochemical workstation in a frequency range of 0.01 Hz–100 kHz and at an amplitude of 5 mV. The open-circuit potential was set as the initial voltage. The rate performance was tested under increasing current densities from 1 to 8 $mA{\cdot}cm^{-2}$ at a given capacity of 1 $mAh{\cdot}cm^{-2}$.

4.4. Fabrication and electrochemical performance tests of Na-air fiber battery

The SCL/Na–air fiber battery exhibited a co-axial structure with a SCL/Na fiber as the anode, a layer of gel electrolyte as the separator, and a flexible CNT film as the cathode.

The fabrication process comprised the following steps. First, sodium metal fiber was wrapped with a CNT film containing absorbed electrolyte. Then, the composite anode was dipped into a precursor solution composed of three components (Solutions A, B, and C) and exposed to ultraviolet irradiation for 15 s to form the gel electrolyte. The coating process was repeated at least three times until the anode was totally covered. The gel electrolyte-coated anode was immersed in Solution D for 12 h. Solution A was 1 M NaTF in diglyme, Solution B was poly(-vinylidene fluoride-*co*-hexafluoropropylene (1 g) dissolved in N-methyl-2-pyrrolidinone (4 g), Solution C was 2-hydroxy-2-methylpropiophenone (0.01 g) dissolved in trimethylolpropane ethoxylate triacrylate (3 g), and Solution D was sodium iodide (0.075 g) and NaTF (1.75 g) dissolved in diglyme (10 mL). Solutions A, B, and C were mixed in a mass ratio of 4:5:3 to prepare the precursor solution of gel electrolyte. All the above samples were prepared in an argon-filled glove box ($H_2O < 0.1$ ppm, $O_2 < 0.1$ ppm). The gel electrolyte-coated SCL/Na fiber anode was then removed from the glove box and wrapped with a CNT film air cathode with a mass loading of 28.2 μg. Finally, the fiber battery was encapsulated sequentially in low-density polyethylene, Parafilm, and a heat-shrinkable tube, which allowed stable battery operation in air by preventing corrosion from ambient moisture/carbon dioxide. For comparison, bare Na–air fiber batteries without SCL were also fabricated. The Na–air fiber batteries were tested in a fixed capacity mode using a specific capacity of 500 $mAh{\cdot}g^{-1}$ and a current density of 1000 $mA{\cdot}g^{-1}$. The specific capacity I was calculated by $C = (I{\times}t)/m$, where I, t, and m represent the discharge/charge current, discharge/charge time, and mass of the air cathode, respectively.

4.5. Fabrication and tests of self-powering strain-sensing system

The self-powering strain-sensing system was constructed with a fiber solar cell energy harvesting unit, a fiber Na–air battery energy storage unit, and a fiber strain sensor. The fiber solar cell was assembled by twisting the Ti/TiO_2 photo-anode and CNT counter electrode and sealing them in a heat-shrinkable tube filled with I^-/I_3^- electrolyte. The fiber strain sensor was assembled by winding an elastic rubber fiber with

polypropylene fibers to form a spring-like polypropylene fiber and coating the spring fiber substrate with CNT conductive ink. The current density–voltage curve of the fiber solar cell was tested by a Newport solar simulator (Oriel Sol 3A, 450 W Xe lamp) under AM 1.5 irradiation (100 $mW{\cdot}cm^{-2}$) and recorded by a Keithley 2400 source meter. The sensing response of the fiber sensor was tested on a CHI 660D electrochemical workstation.

4.6. Finite element method simulations

The Na plating process ($Na^+ + e^- \rightarrow Na$) was simulated by COMSOL Multiphysics 5.4 based on the finite element method. The two physics modules used were "Electrodeposition, Tertiary Nernst-Planck" and "Deformed Geometry Interfaces." The models for cross-sections of the Na–air fiber batteries were established and simulated. For the SCL/Na–air fiber battery, the radius of the Na fiber anode and the thickness of the gel electrolyte were both set at 1 mm. The wavy line indicated the flexible interface between the SCL and the Na fiber anode. For the bare Na–air fiber battery, the sharp protrusions indicated the cracks and creases formed on the bare Na fiber anode during deformation. For the planar Na–air battery, the thickness of the gel electrolyte was set at 1 mm. The initial Na^+ concentration in the electrolyte was set at 1 M. The exchange current density was set to be 1 $A{\cdot}m^{-2}$. The diffusion coefficient of Na^+ in the electrolyte was set at 10^{-9} $m^2{\cdot}s^{-1}$. The ionic mobility, μ, was calculated with the Nernst–Einstein relation. The voltage excitation between the anode and cathode was set at 2 V, and the remaining boundaries were set to be insulated. The concentration-dependent Butler–Volmer equation was used to describe the reaction of Na deposition on the electrode surface.

4.7. Characterizations

SCL/Na and bare Na fiber electrodes were extracted from CR2032 coin cells, washed with diglyme solvent three times to remove residual electrolyte, and dried for 12 h in an argon-filled glove box ($H_2O < 0.1$ ppm, $O_2 < 0.1$ ppm) before characterizations. The structures were characterized by scanning electron microscopy (SEM, Zeiss Gemini SEM500 FESEM operated at 5 kV), transmission electron microscopy (TEM, JEOL JEM-2100F operated at 200 kV), X-ray diffraction (XRD, Bruker AXS D8), Raman spectroscopy (Dilor LabRAM-1B, 4 mW He–Ne laser, excitation wavelength of 532 nm), Fourier transform infrared spectroscopy (FTIR, NICOLET 6700), X-ray photoelectron spectroscopy (XPS, PHI 5000C&PHI5300, Mg, 250 W, 14 kV), and automatic specific surface area and porosity analysis (QUADRASORB evo). The electrochemical performance was tested on a LAND-CT2001A battery tester and a CHI 660D electrochemical workstation. Optical photographs were taken by a camera (Nikon J1). The air-sensitive samples were sealed in an argon-filled box and quickly transferred into the chambers of the test instruments before characterization. For XRD tests, the samples were sealed in Kapton film to avoid side reactions with the air.

Author contributions

H.S. Peng and B.J. Wang proposed the concept. L. Ye and X.R. Cheng performed the experiments. L. Ye, X.R. Cheng, M. Liao, X.M. Sun, B.J. Wang, and H.S. Peng co-wrote the manuscript. All authors participated in data analysis and manuscript discussion.

Declaration of competing interest

The authors declare no competing financial interests.

Acknowledgments

This work was supported by NSFC (52122310, 22075050), STCSM (20JC1414902, 21511104900) and SHMEC (2017-01-07-00-07-E00062).

Appendix A. Supplementary data

Supplementary data to this article can be found online at https://doi.org/10.1016/j.esci.2022.10.001.

References

[1] J. He, C. Lu, H. Jiang, F. Han, X. Shi, J. Wu, L. Wang, T. Chen, J. Wang, Y. Zhang, H. Yang, G. Zhang, X. Sun, B. Wang, P. Chen, Y. Wang, Y. Xia, H. Peng, Scalable production of high-performing woven lithium-ion fibre batteries, Nature 597 (2021) 57–63.
[2] M. Liao, C. Wang, Y. Hong, Y. Zhang, X. Cheng, H. Sun, X. Huang, L. Ye, J. Wu, X. Shi, X. Kang, X. Zhou, J. Wang, P. Li, X. Sun, P. Chen, B. Wang, Y. Wang, Y. Xia, Y. Cheng, H. Peng, Industrial scale production of fibre batteries by a solution-extrusion method, Nat. Nanotechnol. 17 (2022) 372–377.
[3] D.G. Mackanic, M. Kao, Z. Bao, Enabling deformable and stretchable batteries, Adv. Energy Mater. 10 (2020) 2001424.
[4] Z. Khan, M. Vagin, X. Crispin, Can hybrid Na-air batteries outperform nonaqueous $Na\text{-}O_2$ batteries? Adv. Sci. 7 (2020) 1902866.
[5] P. Hartmann, C.L. Bender, M. Vracar, A.K. Durr, A. Garsuch, J. Janek, P. Adelhelm, A comprehensive study on the cell chemistry of the sodium superoxide (NaO_2) battery, Nat. Mater. 12 (2013) 228–232.
[6] J. Ma, F. Meng, Y. Yu, D. Liu, J. Yan, Y. Zhang, X. Zhang, Q. Jiang, Prevention of dendrite growth and volume expansion to give high-performance aprotic bimetallic Li-Na alloy–O_2 batteries, Nat. Chem. 11 (2019) 64–70.
[7] N. Li, D. Xu, D. Bao, J. Ma, X. Zhang, A binder-free, flexible cathode for rechargeable Na-O2 batteries, Chin. J. Catal. 37 (2016) 1172–1179.
[8] X. Liu, X. Lei, Y. Wang, Y. Ding, Prevention of Na corrosion and dendrite growth for long-life flexible Na–air batteries, ACS Cent. Sci. 7 (2021) 335–344.
[9] L. Ye, M. Liao, T. Zhao, H. Sun, Y. Zhao, X. Sun, B. Wang, H. Peng, Stabilizing lithium into cross-stacked nanotube sheets with an ultra-high specific capacity for lithium oxygen batteries, Angew. Chem. Int. Ed. 58 (2019) 17054–17060.
[10] B. Sun, P. Li, J. Zhang, D. Wang, P. Munroe, C. Wang, P.H.L. Notten, G. Wang, Dendrite-free sodium-metal anodes for high-energy sodium-metal batteries, Adv. Mater. 30 (2018) e1801334.
[11] B. Lee, E. Paek, D. Mitlin, S. Lee, Sodium metal anodes: emerging solutions to dendrite growth, Chem. Rev. 119 (2019) 5416–5460.
[12] A. Wang, S. Tang, D. Kong, S. Liu, K. Chiou, L. Zhi, J. Huang, Y. Xia, J. Luo, Bending-tolerant anodes for lithium-metal batteries, Adv. Mater. 30 (2018) 1703891.
[13] H. Sun, G. Zhu, X. Xu, M. Liao, Y. Li, M. Angell, M. Gu, Y. Zhu, W. Hung, J. Li, Y. Kuang, Y. Meng, M. Lin, H. Peng, H. Dai, A safe and non-flammable sodium metal battery based on an ionic liquid electrolyte, Nat. Commun. 10 (2019) 3302.
[14] S. Zhao, C. Wang, D. Du, L. Li, S. Chou, F. Li, J. Chen, Bifunctional effects of cation additive on $Na\text{-}O_2$ batteries, Angew. Chem. Int. Ed. 60 (2021) 3205–3211.
[15] M. Ma, Y. Lu, Z. Yan, J. Chen, In situ synthesis of a bismuth layer on a sodium metal anode for fast interfacial transport in sodium-oxygen batteries, Batteries & Supercaps 2 (2019) 663–667.
[16] M. Zhu, G. Wang, X. Liu, B. Guo, G. Xu, Z. Huang, M. Wu, H. Liu, S. Dou, C. Wu, Dendrite-free sodium metal anodes enabled by a sodium benzenedithiolate-rich protection layer, Angew. Chem. Int. Ed. 59 (2020) 6596–6600.
[17] S. Li, Q. Liu, J. Zhou, T. Pan, L. Gao, W. Zhang, L. Fan, Y. Lu, Hierarchical Co_3O_4 nanofiber–carbon sheet skeleton with superior Na/Li-philic property enabling highly stable alkali metal batteries, Adv. Funct. Mater. 29 (2019) 1808847.
[18] X. He, Y. Ni, Y. Li, H. Sun, Y. Lu, H. Li, Z. Yan, K. Zhang, J. Chen, An MXene-based metal anode with stepped sodiophilic gradient structure enables a large current density for rechargeable Na–O_2 batteries, Adv. Mater. 34 (2022) 2106565.
[19] A. Parejiya, R. Amin, R. Essehli, D.L. Wood, I. Belharouak, Improving contact impedance via electrochemical pulses applied to lithium–solid electrolyte interface in solid-state batteries, ACS Energy Lett. 5 (2020) 3368–3373.
[20] G. Li, Z. Liu, Q. Huang, Y. Gao, M. Regula, D. Wang, L. Chen, D. Wang, Stable metal battery anodes enabled by polyethylenimine sponge hosts by way of electrokinetic effects, Nat. Energy 3 (2018) 1076–1083.
[21] X. Zhong, Y. Li, Y. Liu, X. Qiao, Y. Feng, J. Liang, J. Jin, L. Zhu, F. Hou, J. Li, Continuous multilayered carbon nanotube yarns, Adv. Mater. 22 (2010) 692–696.
[22] L. Ye, M. Liao, H. Sun, Y. Yang, C. Tang, Y. Zhao, L. Wang, Y. Xu, L. Zhang, B. Wang, F. Xu, X. Sun, Y. Zhang, H. Dai, P.G. Bruce, H. Peng, A sodiophilic interphase-mediated, dendrite-free anode with ultrahigh specific capacity for sodium-metal batteries, Angew. Chem. Int. Ed. 58 (2019) 2437–2442.
[23] C.L. Bender, B. Jache, P. Adelhelm, J. Janek, Sodiated carbon: a reversible anode for sodium–oxygen batteries and route for the chemical synthesis of sodium superoxide (NaO_2), J. Mater. Chem. 3 (2015) 20633–20641.
[24] H. Wang, J. Hu, J. Dong, K.C. Lau, L. Qin, Y. Lei, B. Li, D. Zhai, Y. Wu, F. Kang, Artificial solid-electrolyte interphase enabled high-capacity and stable cycling potassium metal batteries, Adv. Energy Mater. 9 (2019) 1902697.
[25] R.V. Salvatierra, G.A. Lopez-Silva, A.S. Jalilov, J. Yoon, G. Wu, A.L. Tsai, J.M. Tour, Suppressing Li metal dendrites through a solid Li-ion backup layer, Adv. Mater. 30 (2018) e1803869.
[26] P. Liu, H. Yi, S. Zheng, Z. Li, K. Zhu, Z. Sun, T. Jin, L. Jiao, Regulating deposition behavior of sodium ions for dendrite-free sodium-metal anode, Adv. Energy Mater. 11 (2021) 2101976.
[27] B. Jache, P. Adelhelm, Use of Graphite as a highly reversible electrode with superior cycle life for sodium-ion batteries by making use of co-intercalation phenomena, Angew. Chem. Int. Ed. 53 (2014) 10169–10173.

[28] G. Zheng, Q. Lin, J. Ma, J. Zhang, Y. He, X. Tang, F. Kang, W. Lv, Q. Yang, Ultrafast presodiation of graphene anodes for high-efficiency and high-rate sodium-ion storage, InfoMat 3 (2021) 1445–1454.
[29] L. Wang, J. Shang, Q. Huang, H. Hu, Y. Zhang, C. Xie, Y. Luo, Y. Gao, H. Wang, Z. Zheng, Smoothing the sodium-metal anode with a self-regulating alloy interface for high-energy and sustainable sodium-metal batteries, Adv. Mater. 33 (2021) e2102802.
[30] W. Liu, D. Lin, A. Pei, Y. Cui, Stabilizing lithium metal anodes by uniform Li-ion flux distribution in nanochannel confinement, J. Am. Chem. Soc. 38 (2016) 15443–15450.
[31] W. Yin, Z. Shadike, Y. Yang, F. Dong, L. Sang, H. Li, Z. Fu, A long-life Na–air battery based on a soluble NaI catalyst, Chem. Commun. 51 (2015) 2324–2327.
[32] L. Wang, J. Pan, Y. Zhang, X. Cheng, L. Liu, H. Peng, A Li–air battery with ultralong cycle life an ambient air, Adv. Mater. 30 (2018) 1704378.